

We are IntechOpen, the world's leading publisher of Open Access books Built by scientists, for scientists

6,900

Open access books available

186,000

International authors and editors

200M

Downloads

Our authors are among the

154

Countries delivered to

TOP 1%

most cited scientists

12.2%

Contributors from top 500 universities



WEB OF SCIENCE™

Selection of our books indexed in the Book Citation Index
in Web of Science™ Core Collection (BKCI)

Interested in publishing with us?
Contact book.department@intechopen.com

Numbers displayed above are based on latest data collected.
For more information visit www.intechopen.com



Transition Metal Chalcogenide (TMC) Nanocomposites for Environmental Remediation Application over Extended Solar Irradiation

Sivagowri Shanmugaratnam and Shivatharsiny Rasalingam

Abstract

Demand for environmental protection is gaining more public attention and legislative support. The development in industrial and technological sectors results in severe environmental issues, such as environmental contamination and energy shortage. Therefore, the development of new nanocomposites that can effectively act toward environmental remediation is necessary to overcome the detrimental environmental impacts. Transition metal chalcogenides (TMC) have gained worldwide attention in recent decades and are being researched for use in different applications due to their indirect bandgaps, optoelectronic behavior, and their stability that can enable the catalysts to absorb visible light that is abundant in solar radiation. In this chapter, synthesis, characterization, and application of TMCs, such as MS_x and MSe_x , toward environmental remediation application are reviewed. Efficiency of different TMC materials and different experimental conditions is also elaborated.

Keywords: transition metal chalcogenides, degradation, hydrothermal, organic compounds

1. Introduction

Effluents of industrial wastes are the important source of water pollution that are toxic in the environment and are becoming the biggest problem that influence the survival of human beings and other creatures in the environment. The demand of clean water is increasing with the rapid growth of global population; in the present, several treatment techniques that include biodegradation, membrane process, coagulation, adsorption, precipitation, sonochemical degradation, micellar-enhanced ultrafiltration, and advanced oxidation process (AOP) have been utilized to remove pollutants from wastewater [1]. Among them, AOP is an efficient method to remove the contaminants that are not degradable by means of biological processes. Since these processes involve the production of very reactive oxygen

species (ROS), it can be able to destroy a wide range of organic compounds. A wide range of semiconductor photocatalysts have been utilized in AOPs. The first photocatalyst, TiO_2 , discovered by Fujima and Honda in 1972 was found as gold standard due to its significant characteristics that include high chemical stability, nontoxicity, and relatively low price [2]. However, it only absorbs ultraviolet irradiation from sunlight due to its wide bandgap. To overcome this problem, several studies are focusing on finding ways to extend the absorption wavelength range of TiO_2 . In this regard, metal or nonmetal elements doped onto TiO_2 and visible light response photocatalysts are being developed as the future generation. Among which transition metal chalcogenide (TMC) materials gained worldwide attention in recent decades because of their significant characteristics, such as excellent optical absorption due to its tunable indirect bandgap energies (1–2 eV) [3]. Moreover TMCs with graphene oxides [4], carbon nitride [5], metal oxides [6], and metals [7] were found to increase the conductivity of electrons, provide active sites, and effectively separate the electron and hole pairs generated by the semiconductor photocatalysts [4]. This chapter explores the synthesis, characterization, and the applications of TMCs.

2. Transition metal chalcogenides (TMCs)

Transition metal chalcogenides are considered as emerging candidates due to their unique physical and chemical properties and are being researched for use in lithium-ion batteries, solar cells, hydrogen evolution, and photocatalytic degradation due to their indirect bandgaps, optoelectronic behavior, and stability. In addition, nanodots (quantum dots)/nanostructures of these metal chalcogenides show stronger edge effects, and the quantum confinement effect makes it possible to utilize under solar-simulated irradiation [8, 9].

2.1 Different preparation methods

There are several methods to synthesize transitional metal chalcogenides, including ultrasonic chemical method, hydrothermal method, simple template-free one-pot method, an ion-exchange and precipitation methods, simple microwave-assisted solvothermal process, and surface modification method [5–12]. The following sections explore the most common preparation methods of TMCs.

Hydrothermal reaction usually occurs in the reaction vessel of stainless steel autoclave. The presence of aqueous solution or mineralizers under high pressure and low temperature encourages interaction of precursor materials during the process. This method has the feature to make high crystalline nanostructures or products at relatively low temperature [13, 14]. A range of TMCs that include NiS [15], CuS , FeS_2 , NiS_2 [10], etc. have been synthesized using hydrothermal treatment method due to low temperature requirement (150°C), short time duration (~ 4 h), and high yield ($>90\%$). In addition, there is no need to use any complexing agents or no need to control the pH [10] (**Figure 1**).

Further, hydrothermal method has been utilized to synthesize TMC-doped metal [16], metal oxides [17], or carbonaceous [18] materials. The following schematic illustration represents the preparation of CdS nanosheet-RGO hybrid material using hydrothermal treatment method (**Figure 2**).

Apart from these, microwave-assisted synthesis method has also been used to prepare TMCs with controllable size and shape compared with conventional heating method due to the homogeneous heating process. Further, this method can promote nucleation and, thus, reduce the time required for synthesis [18].



Figure 1.
Schematic illustration of the hydrothermal synthesis of FeS_2 , CuS , and NiS_2 powders. Reproduced with permission from [10].

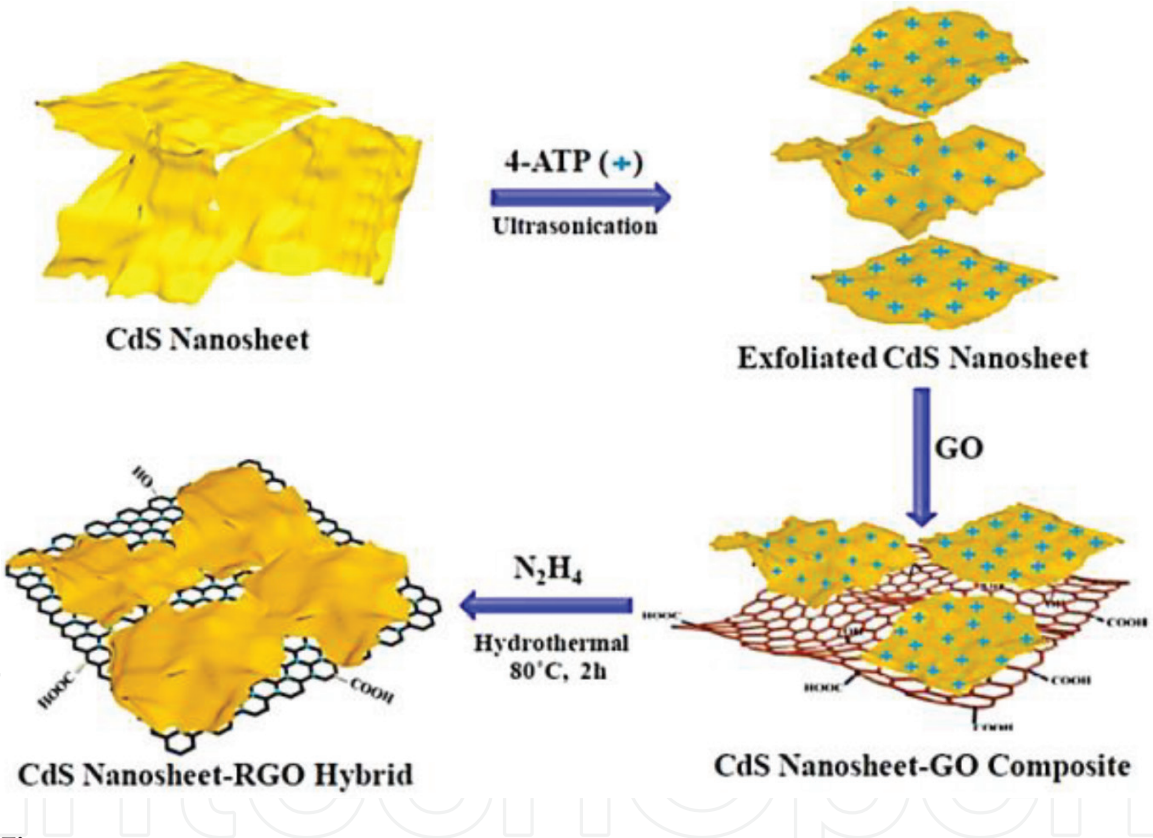


Figure 2.
Synthesis of CdS nanosheet-RGO hybrid. Reproduced with permission from [18].

Simple template-free one-pot method is a simple synthetic approach that was used to develop certain metal oxide hollow spheres based on direct solid evacuation arising from Ostwald ripening, the Kirkendall effect, or chemically induced self-transformation [19].

Figure 3 illustrates the mechanism for the simple template-free one-pot method to prepare hollow sphere, Ni-doped CdS material. Herein, biomolecular glutathione was used as sulfur and bubble source [7].

2.2 Characterization techniques for transition metal dichalcogenides

The essential techniques used to characterize the transition metal chalcogenide materials are discussed in this section.

2.2.1 X-ray diffraction spectroscopy

X-ray diffraction (XRD) spectroscopy is a nondestructive method used to analyze the crystallinity, crystal structure, crystallite size, and phase composition of the photocatalytic materials which presents in powder form or thin film.

In the study by Li and co-workers, MoS₂ nanosheets coupled into the carbon nitride to form MoS₂/C₃N₄ heterostructures synthesized by a facile ultrasonic chemical method were characterized by using XRD. All the samples prepared



Figure 3.
Mechanism for the formation of Ni-doped CdS. Reproduced with permission from [7].

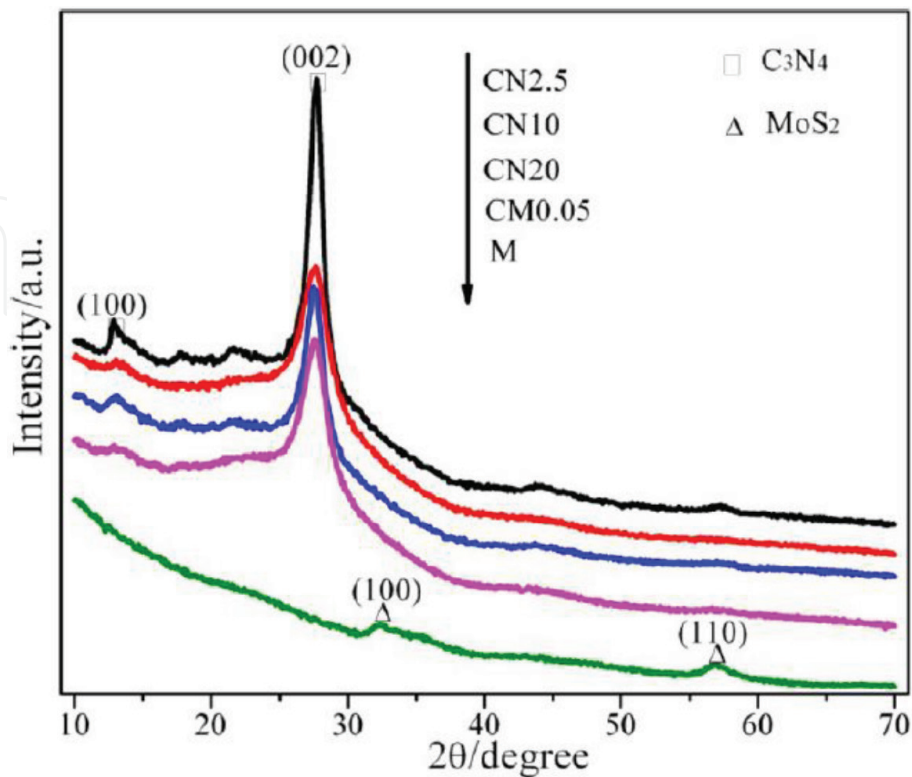


Figure 4.
XRD pattern for MoS₂ on g-C₃N₄ in different amounts. Reproduced with permission from [5].

showed similar patterns, and the peaks at 32.6 and 58.3° were assigned to the (100) and (110) crystal plane formation of MoS₂. Peak at 27.4° indicated to the (002) stacking layered structure, while the 13.0° peak corresponds to the (100) in-plane repeated units. The observation from XRD confirms the formation of MoS₂/C₃N₄ heterostructure [5] (**Figure 4**).

In another study, NiS nanoparticles prepared hydrothermally were characterized by powder XRD method.

Figure 5 illustrates the XRD patterns of as-prepared nanostructured NiS samples. The patterns were indexed to rhombohedral structured NiS with the space group of R3m. The cell parameters were found to be $a = 9.61 \text{ \AA}$ and $c = 3.16 \text{ \AA}$ [15].

XRD pattern (**Figure 6**) confirmed the formation of CdS, and Ni-doped CdS materials prepared by one-pot synthesis method show similar pattern and are assigned to hexagonal phase. It was also found that the peak intensity increases with the increase in Ni²⁺ doping concentration. Average crystallite size was estimated based on the broadening of the (002) peak, and it was found that the crystallite size also increased with the %Ni doped on CdS [7].

X-ray powder diffraction patterns of different metal sulfides were reported by Ali and co-workers as illustrated in **Figure 7**. The diffraction patterns of the samples are indexed to pyrite FeS₂, covellite CuS, and vaesite NiS₂. The purity of the phases was confirmed by the absence of additional peaks in their XRD. XRD patterns of cubic FeS₂ and NiS₂ were found to be isostructural, whereas CuS was found in a hexagonal symmetry. The crystallite sizes of the materials were estimated as 50, 45, and 22 nm for FeS₂, CuS, and NiS₂, respectively [10].

2.2.2 Electron microscopy

Scanning electron microscopy (SEM) is one of the electron microscopic techniques that images the sample surface using high beam electrons. In this technique, beam electrons strike the surface of the specimen and interact with atoms and form the secondary electrons, which characterized the information about the

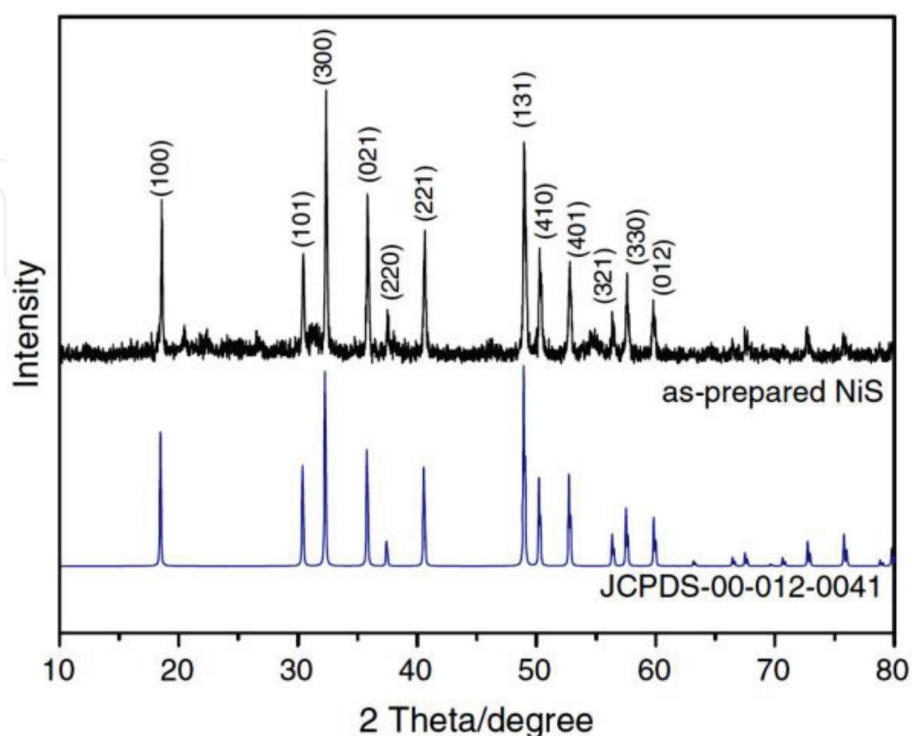


Figure 5.
XRD for synthesized NiS. Reproduced with permission from [15].

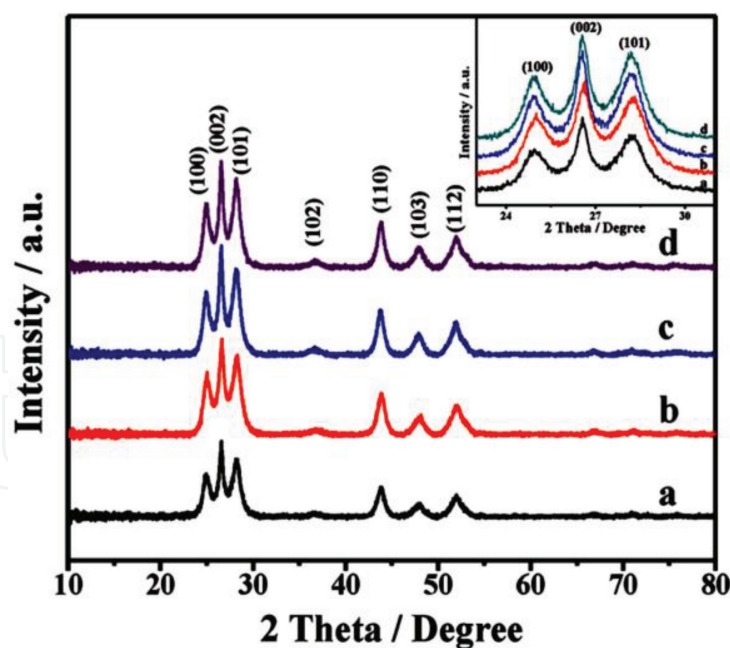


Figure 6.
XRD for Ni doped on CdS. Reproduced with permission from [7].

morphology of sample surface in high-resolution images colored in black and white. SEM is used to view dispersion of nanoparticles in different nanostructures, such as nanotubes, nanoclays, nanofillers, and nanofibers. In addition, the method used X-ray to identify elemental composition known as energy-dispersive ray method (EDX). The transmission electron microscopy (TEM) images form when beam of electron is transmitted through the sample and magnified by objective lens. This technique is the most preferred to measure the particle size and thickness of sample. In particular, for the morphology of materials, monitoring morphology and dispersion is very crucial compared to scanning electron microscopy [20].

Figure 8(a) shows SEM images of carnation flowerlike morphology with a diameter of about 500–700 nm. **Figure 8(b) and (c)** is the magnified view of an individual SnS_2 flower containing ultrathin nanopetals as building blocks, which is in 10 nm thick. These building blocks linked together and form 3D flowerlike structure. **Figure 8(d) and (e)** shows the TEM images of dense core of SnS_2 flower structure that clearly indicates that the nanopetals are well arranged across the flower center; however, the nanopetals of SnS_2 were not connected together. Finally, **Figure 8(f)** shows nanoparticles in randomly arranged manner with uneven sizes [21].

In the green synthesis of earth-abundant metal sulfides by Ali and co-workers, the samples prepared exhibited uniform morphology and particle size distribution, which is due to a controlled growth during the hydrothermal synthesis. The presence of iron, copper, nickel, sulfur, and carbon and its purity obtained using SEM analysis was found to be in good agreement with the phases observed by XRD. In addition, the atomic content of Fe, Cu, Ni, and S in the samples had a good correlation with theoretical atomic% of all the phases. The morphological analysis confirmed that as-prepared sulfides are in the form of agglomerated particles. In addition, polyhedral particles with the size of $\sim 676 \pm 44$ nm were obtained for FeS_2 sample, whereas CuS and NiS_2 exhibited irregular- and spherical-shaped particles with the size of $\sim 783 \pm 53$ and 933 ± 68 nm, respectively [10] (**Figure 9**).

Li et al. studied the morphology and microstructure of the as-prepared samples of WS_2 by using SEM and TEM. The detailed structural information of the $\text{WS}_2/\text{Bi}_2\text{MoO}_6$ composite was obtained by TEM analysis, and an irregular platelet-shaped nanostructure was observed with the length ranging from 500 nm to 2 μm .

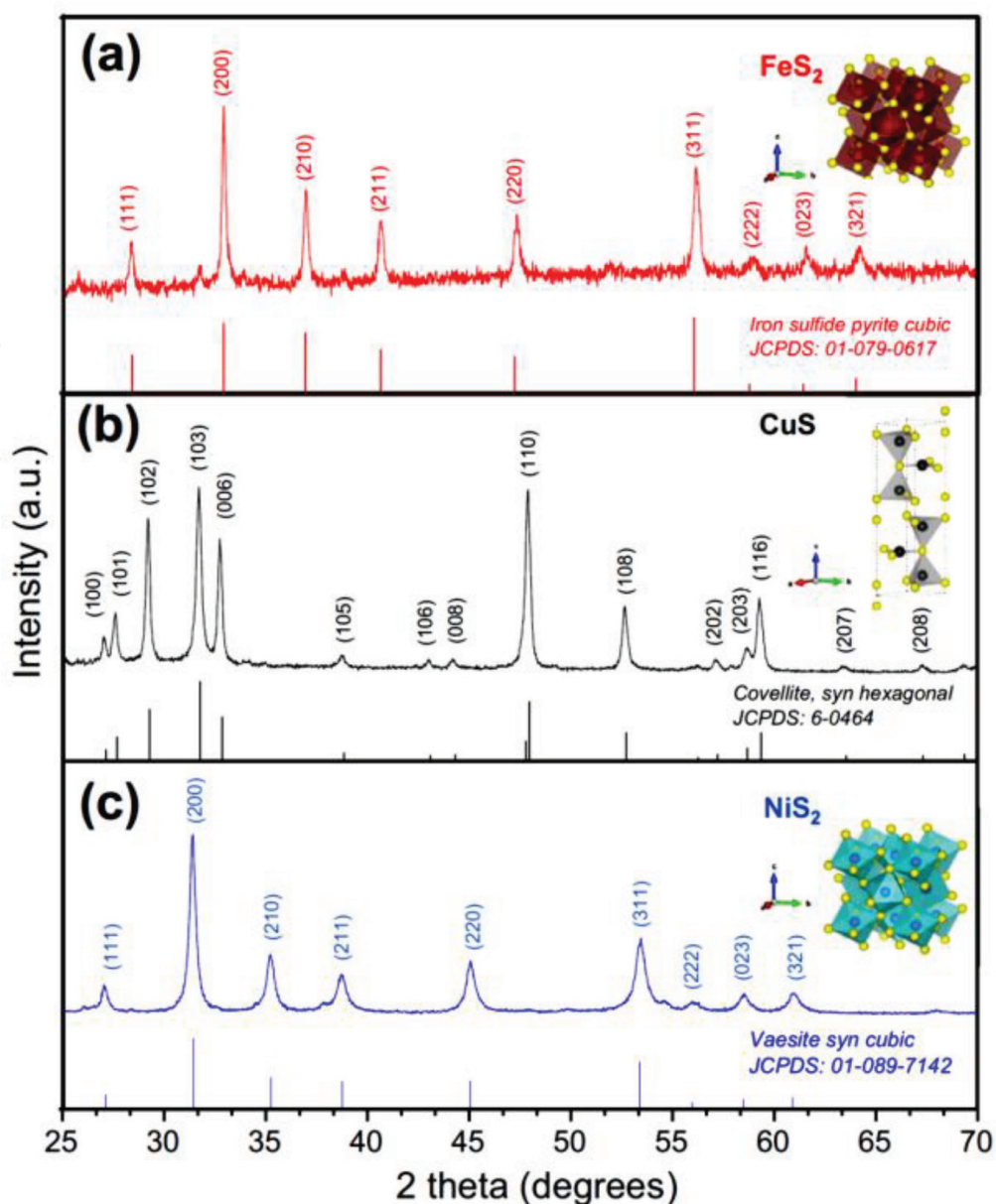


Figure 7.
 XRD diffraction patterns and schematic representations of the crystalline structure of (a) FeS_2 , (b) CuS , and (c) NiS_2 . Reproduced with permission from [10].

The results obtained from TEM were in good agreement with SEM analysis. The HRTEM of the prepared materials further confirm the nanojunction structure.

Figure 10 illustrates two sets of different lattice images with the lattice fringe of 0.27 and 0.46 nm obtained from TEM corresponded to the (100) plane of WS_2 and (120) plane of Bi_2MoO_6 resulted from the XRD [17].

2.2.3 X-ray photoelectron spectroscopy

XPS or X-ray photoelectron spectroscopy is used as surface analytic technique based on the photoelectric effect. XPS is mainly used to find the composition of elements in the surface of the materials and to determine the valence band structure and chemical state of components.

Figure 11(a) illustrates the XPS molybdenum 3d spectra for MoSe_2 , which exhibit peaks on 228.84 and 232.01 eV indicating binding energy of $\text{Mo } 3d_{5/2}$ and $\text{Mo } 3d_{3/2}$ for Mo^{4+} ions, respectively. In addition, **Figure 11(c)** depicts the XPS of MoSe_x (at 120°C) indicating additional peaks at 232.07 and 229.45 eV which can be

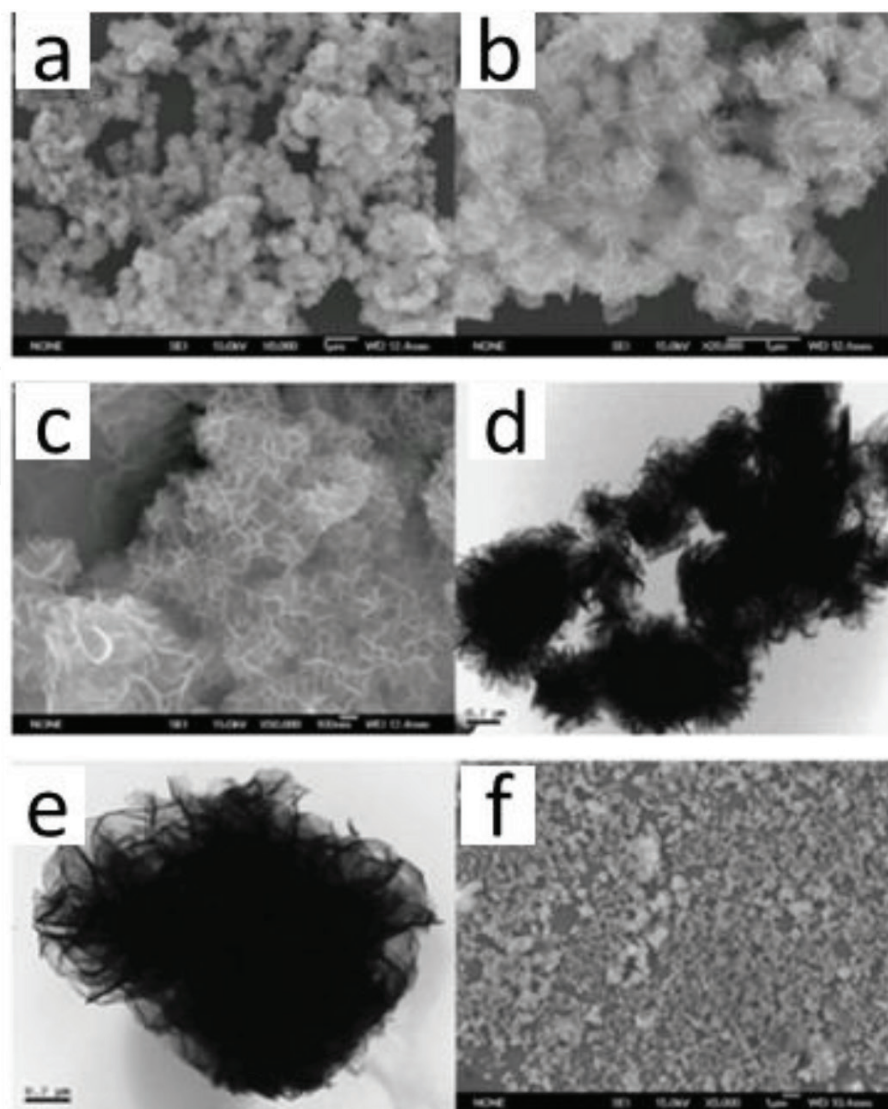


Figure 8.

(a–c) SEM images of SnS_2 flowerlike structure, (d–e) TEM images of SnS_2 flowerlike structure, and (f) SEM images of SnS_2 nanoparticles. Reproduced with permission from [21].

attributed to the binding energy of Mo^{5+} ions. The results confirmed the synthesis at 120°C , which resulted in two chemical states (IV and V) of molybdenum. Further, it was found that the amorphous MoSe_2 showed a very broad Se 3d peak than the crystalline MoSe_2 . The Se $3d_{5/2}$ and Se $3d_{3/2}$ peaks for amorphous and crystal samples of MoSe_2 were found to lie between the range of 52 and 57 eV; however, the intensity of the peaks varied in amorphous sample. Peak-fitting analysis showed that the ratio of Mo to Se in the amorphous MoSe_x sample was 1:3:1 [3].

Figure 12(a) shows the schematic of PtSe_2 in monolayer format, in that one sublayer of Pt atoms is sandwiched between two Se sublayers. **Figure 12(b)** shows the XPS measurements for Se during the growth of PtSe_2 at 270°C . The peaks at 55.68 and 54.80 eV indicate the binding energy of Se(0) chemical state at 25°C , and at 270°C , the peaks were found at 55.19 and 54.39 eV corresponding to the binding energy of Se^{2-} chemical state; in between that, at 200°C , the curve indicates the coexistence of Se(0) and Se^{2-} states. The binding energies of Se confirmed the formation of PtSe_2 at 270°C [22].

The XPS survey spectrum of SnS_2 -AP (**Figure 13**) confirmed the presence of Sn and S components, whereas Cr, C, and O were found to be the contaminants. High-resolution XPS spectra of Sn 3d and S 2p core levels proved that the binding energies of Sn 3d and S 2p of SnS_2 -AP were very close to those of SnS_2 -(c). The binding

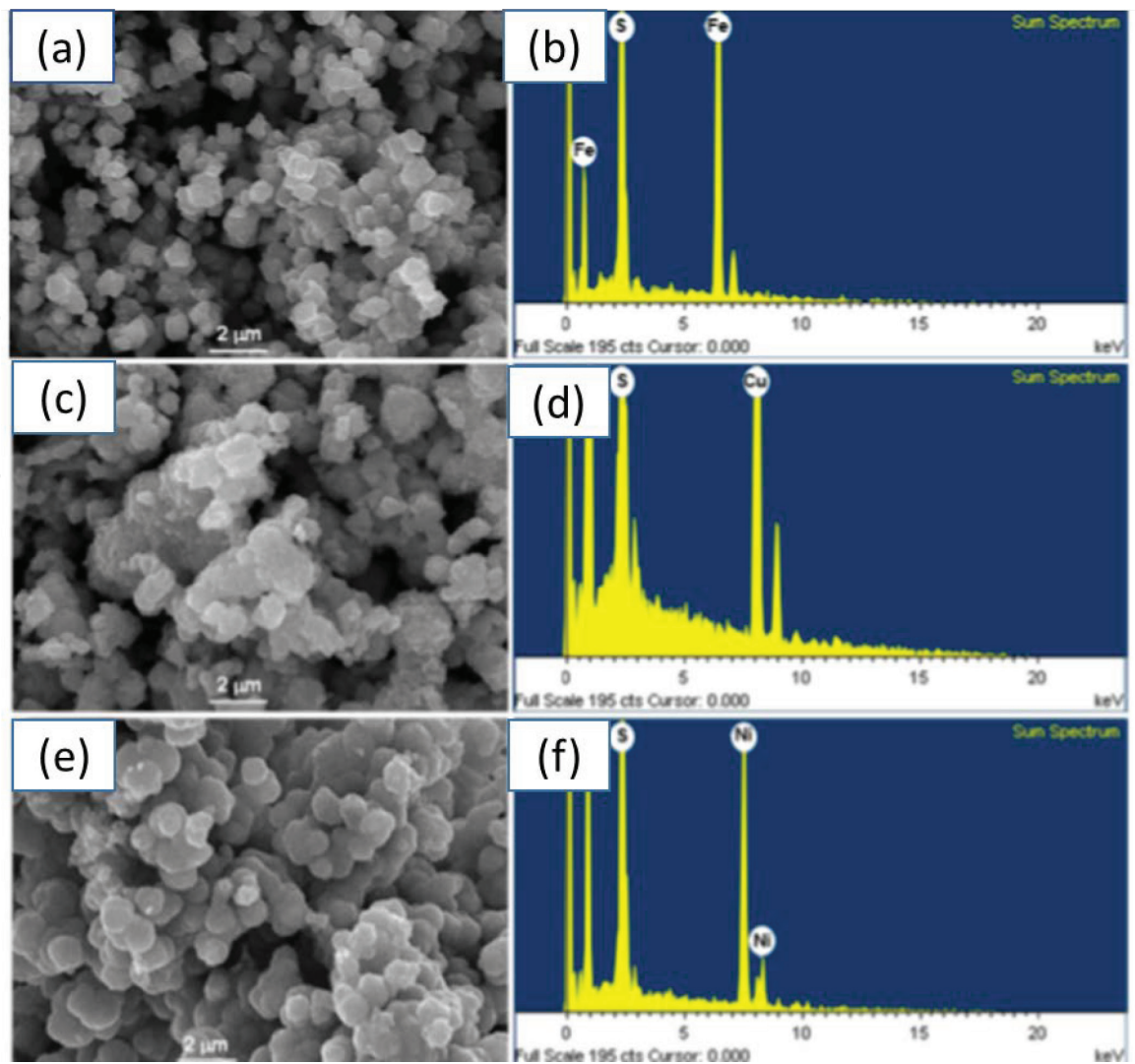


Figure 9.
SEM and EDS analysis of (a, b) FeS₂, (c, d) CuS, and (e, f) NiS₂. Reproduced with permission from [10].

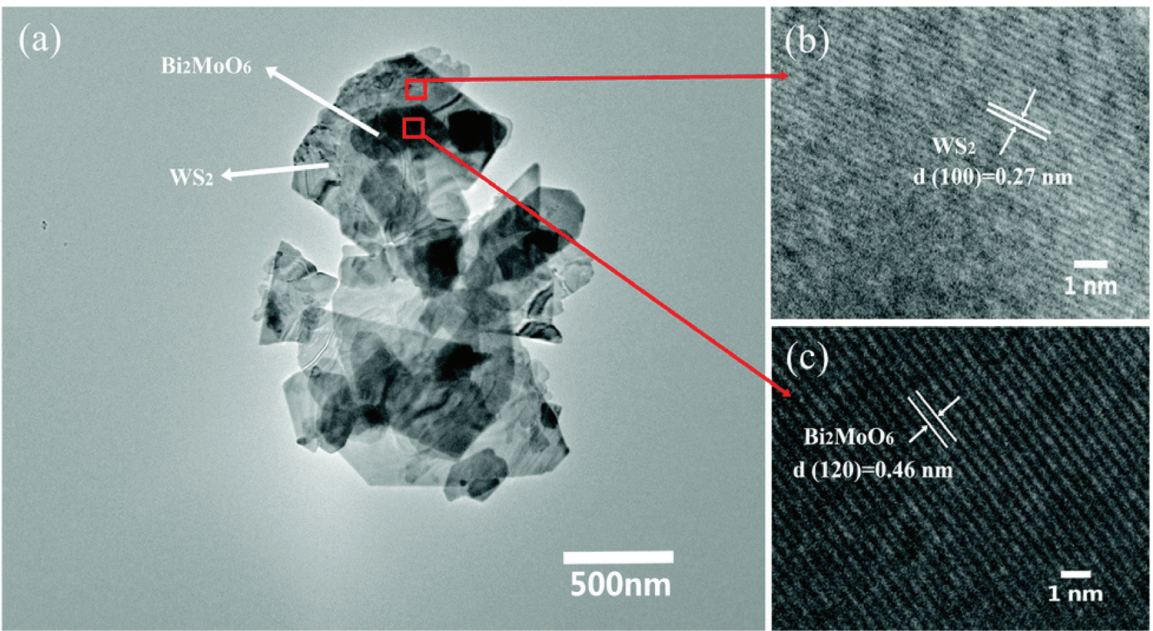


Figure 10.
TEM and HRTEM images of the hierarchical WS₂/Bi₂MoO₆ composite (5 wt% of WS₂). Reproduced with permission from [17].

energies of Sn 3d_{5/2} and S 2p_{3/2} of SnS₂-AP and SnS₂-(c) were 486.61 and 486.65, 161.68, and 161.74 eV, respectively. It was also found that the binding energies of Sn 3d_{5/2} and S 2p_{3/2} of SnS₂-AP and SnS₂-(c) were of close proximity with the reference data of Sn⁴⁺ and S²⁻ in SnS₂.

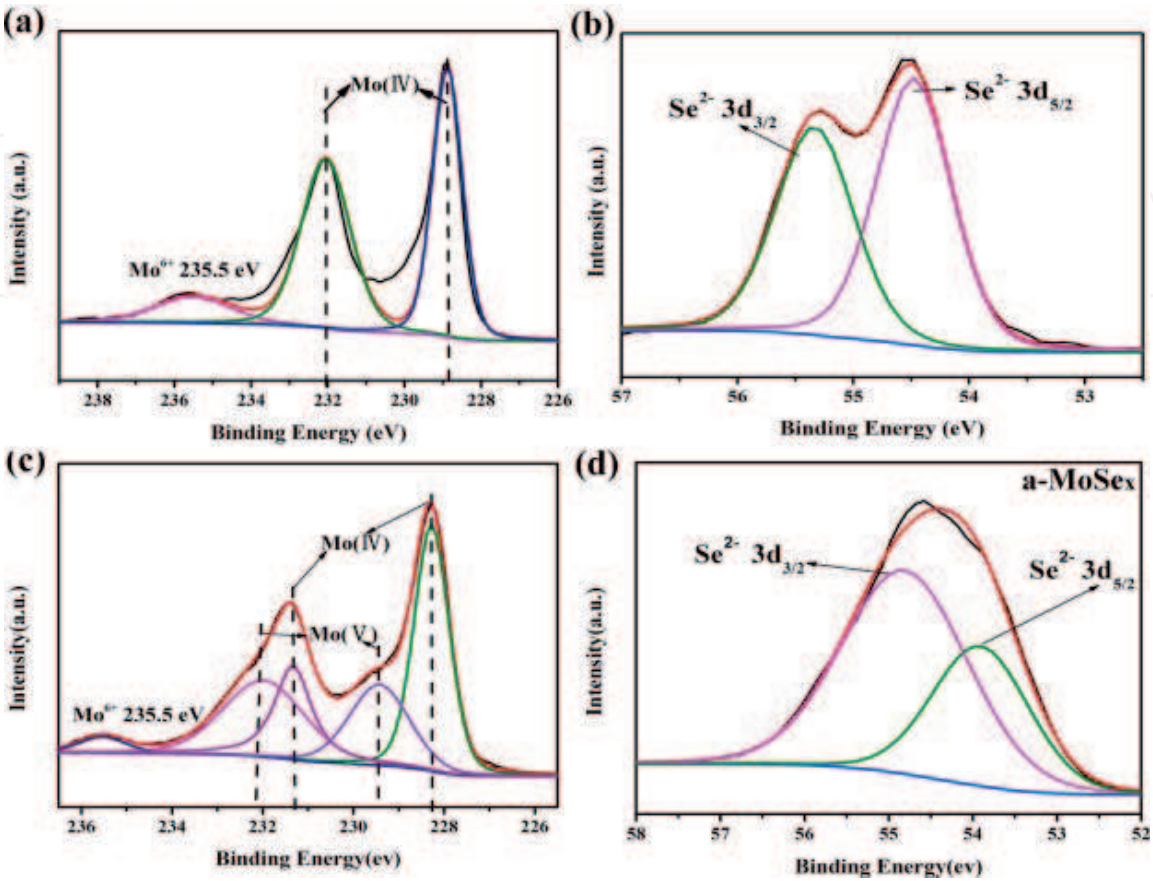


Figure 11. (a, b) XPS for MoSe₂, (c, d) XPS for MoSe_x. Reproduced with permission from [3].

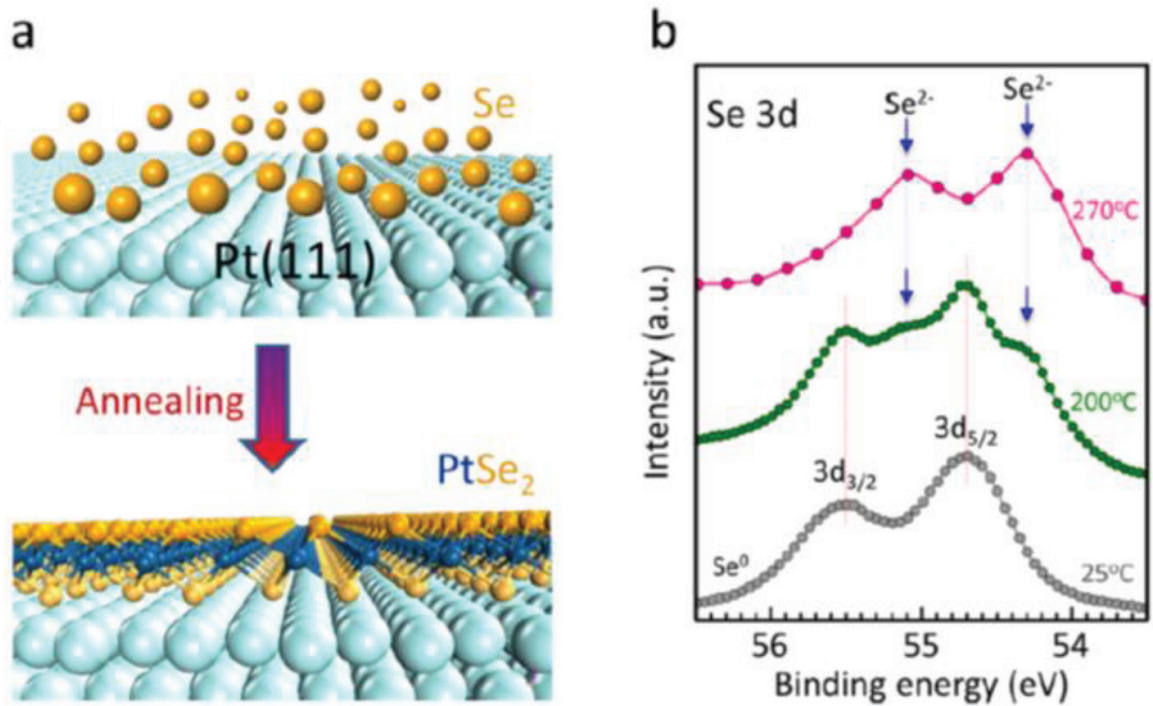


Figure 12. (a) PtSe₂ monolayer and (b) XPS for PtSe₂. Reproduced with permission from [22].

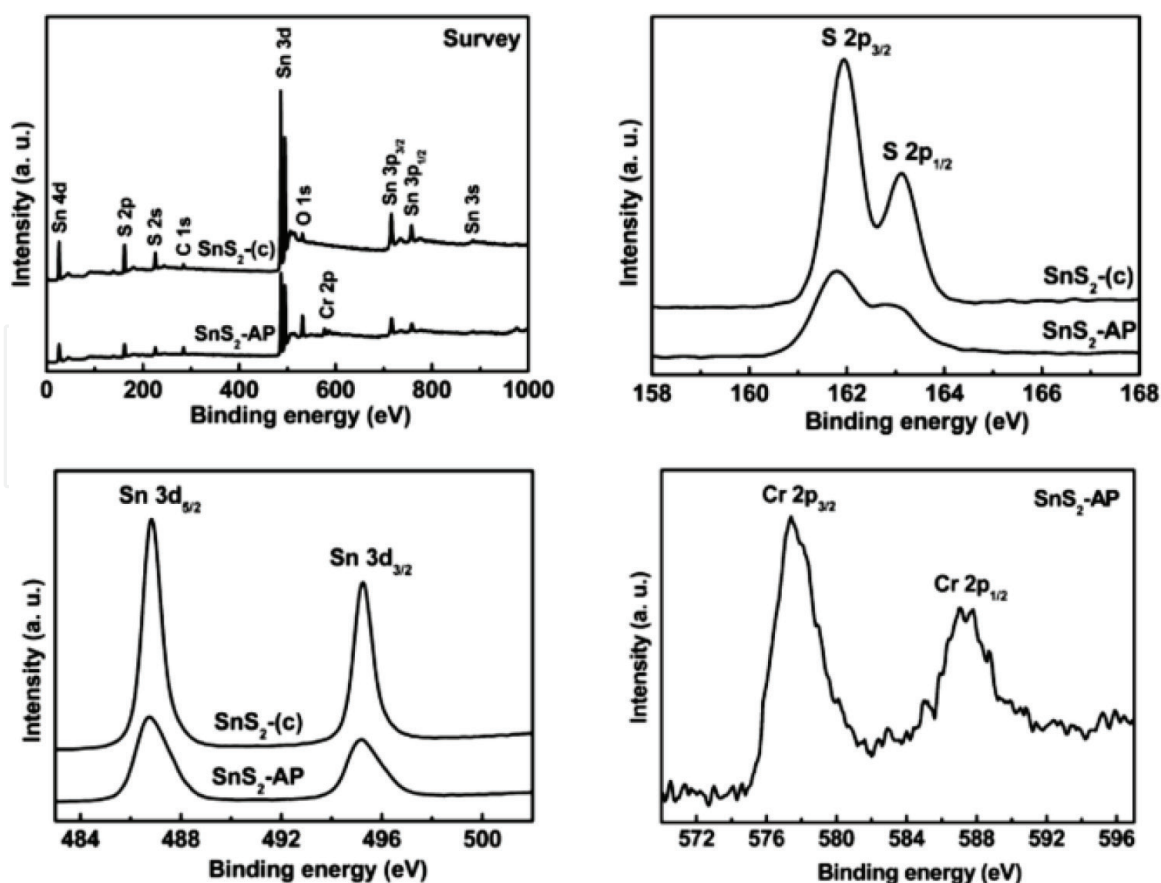


Figure 13.
 XPS spectra of $\text{SnS}_2\text{-AP}$ and $\text{SnS}_2\text{-(c)}$. Reproduced with permission from [23].

Apart from these, a peak attained at 577.36 eV is due to the binding energy of Cr $2p_{3/2}$ corresponding to Cr (III) in $\text{Cr}(\text{OH})_3$. The hydrolysis-precipitation of Cr(III) ion leads to the formation of $\text{Cr}(\text{OH})_3$ on the surface of $\text{SnS}_2\text{-AP}$. Cr(III) were generated from the photocatalytic reduction of adsorbed Cr(VI) [23].

2.3 Photodegradation of organics using TMCs

Persistent organic pollutants (POPs) are of global concern because of their potential for long-range transport, persistence in the environment, ability to biomagnify and bioaccumulate in ecosystems, as well as possess negative effects on human health and the environment. In particular, the agrochemicals and textile effluents involve processes that produce compounds that are very toxic to the environment. Thus, it is necessary to remove these colored pollutants from the environment. Several catalysts have been utilized to remove the pollutants from the polluted environment, and the transition metal chalcogenide has recently gained much attention in this regard due to their significant characteristic properties.

Wen-chao Peng et al. synthesized MoS_2 /reduced graphene oxide hybrid with CdS nanoparticle for photocatalytic reduction of nitroaromatic compounds to aromatic amines under visible light irradiation in the presence of sacrificial agent. It was also noted that composite of CdS-0.03 (MoS_2 /0.01rGO) exhibited remarkable enhancement on the 4-nitrophenol reduction due to the separation of electron-hole pairs generated by CdS nanoparticles [4] (Figure 14). In addition, it was found that the photocatalyst appeared to be stable confirmed by recycling study as illustrated in the following figure.

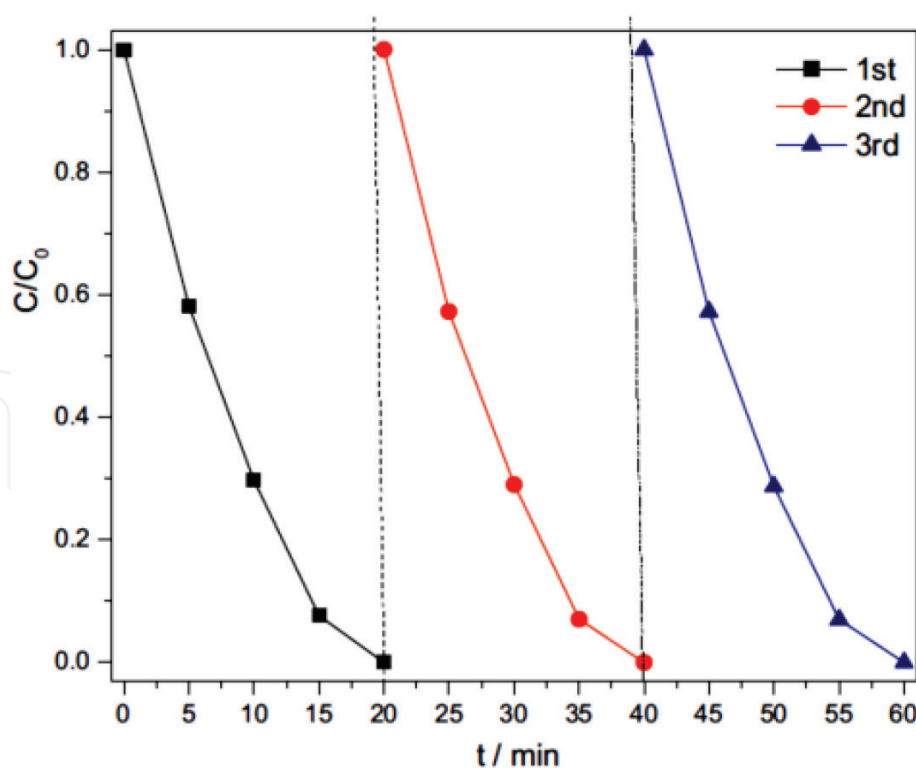


Figure 14.

Repeated tests using recycled CdS 0.03(MoS₂/0.01rGO) composite catalyst for photocatalytic 4-nitrophenol reduction. Reproduced with permission from [4].

In another study, Peitao Liu and co-workers worked on prepared N-doped MoS₂ nanoflowers (specific surface area of 114.2 m² g⁻¹) and α-Fe₂O₃@N-doped MoS₂ heterostructures for decoloring or the removal of the Rhodamine B (RhB) under visible light irradiation. When comparing the activity of these two materials, N-doped MoS₂ nanoflowers showed optimum rate constant as 0.0928 min⁻¹, which was 26.4 times greater than that of MoS₂ nanosheets. Further, 20 mg of these catalysts completely degraded the 50 mL of 30 mgL⁻¹ RhB within 70 min [24] (**Figure 15**).

MoS₂ nanosheets were coated into carbon nitride synthesized by facile ultrasonic chemical method to form heterostructures. These materials were used to explore the photocatalytic degradation of the dyes, RhB and MO, and the optimum reaction rate constant was found to be 301 min⁻¹ with the 0.05 wt% MoS₂ [5].

Yangyang Liu and co-workers synthesized ZnO nanosheet doped with P by using conventional chemical vapor transport and condensation (CVTC) method and then coated with an atomic layer of MoS₂ on it (**Figure 16**).

The photocatalytic activity of the catalyst was tested by degradation of organic dyes, such as methylene blue (MB) and Rhodamine B (RhB), under natural sunlight. It was found that 95% of organic dyes were degraded within 6 min and photocatalytic rate constant was found to be 1.413 min⁻¹, which was 3.4 times better than that of P25 due to the enhanced light adsorption efficiency obtained by synergetic effect of MoS₂ [6].

In another study, Haiyang Liu et al. worked on 1 T@2H-MoS₂/Ag composite synthesized by microwave-hydrothermal and photoreduction methods for photocatalytic degradation of conventional dyes and photocatalytic reduction of Cr(VI) under visible light irradiation. It was observed that 1 T@2H-MoS₂/Ag effectively enhanced photocatalytic activity compared with 2H-MoS₂ due to the enhancement in the light response range and charge separation by using Ag quantum dots and 1 T phase. In addition, 1 T@2H-MoS₂ showed 81 and 41% of increment in

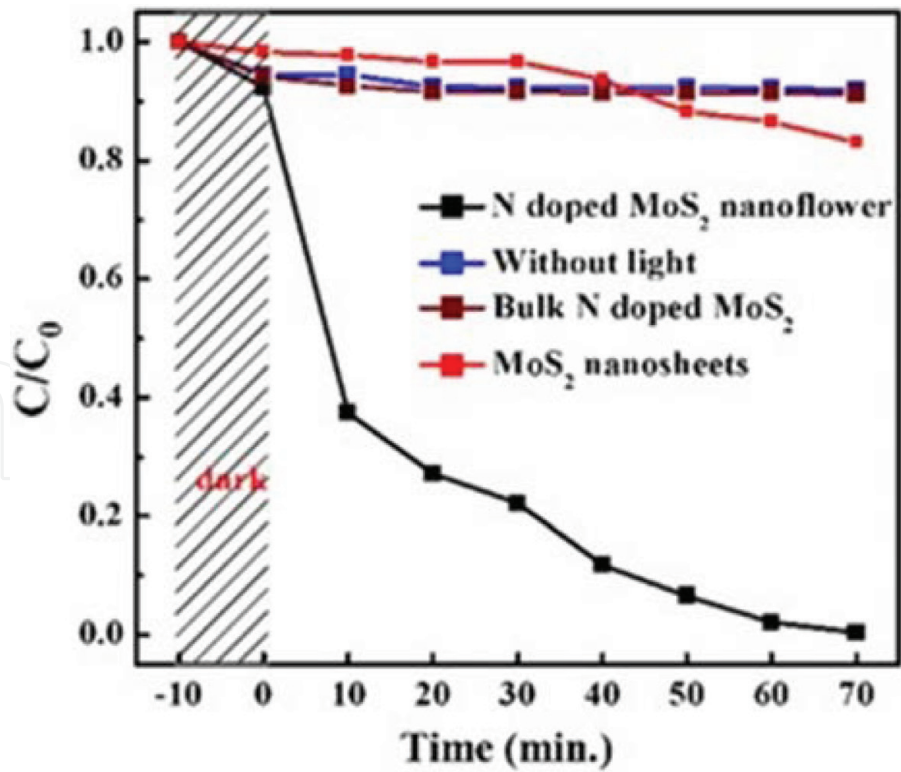


Figure 15. Photocatalytic degradation of RhB by different photocatalysts (N-doped MoS₂ nanoflower; without light, bulk N-doped MoS₂, and MoS₂ nanosheets) under visible light irradiation, where C and C₀ are the RhB concentrations at time t min. And 0 min, respectively. Reproduced with permission from [24].

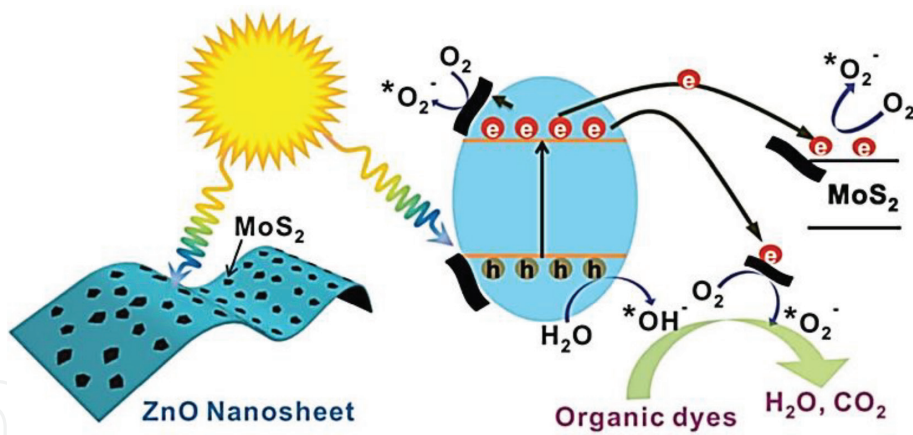


Figure 16. Mechanism of photolysis on ZnO decorated with MoS₂. Reproduced with permission from [6].

photocatalytic reduction of Cr(VI) and photocatalytic degradation of methylene blue, respectively [16] (**Figure 17**).

In a different study, Xi Yang et al. worked on amorphous and crystalline molybdenum selenide synthesized by facile low-temperature hydrothermal method for adsorption and degradation of Rhodamine and methylene blue under dark and visible light irradiation. Due to the excellent optical absorption and narrow bandgap (1–2 eV), molybdenum selenide (MoSe₂) is preferred for the photocatalytic degradation of pollutants. Hole and free radical studies concluded that the photocatalytic effect of the amorphous samples was higher than that of the crystalline samples due to the different active substances. The active substances, superoxide radicals, in particular, predominated the process of degrading the dye. When comparing the amorphous and crystalline materials, amorphous molybdenum selenide showed

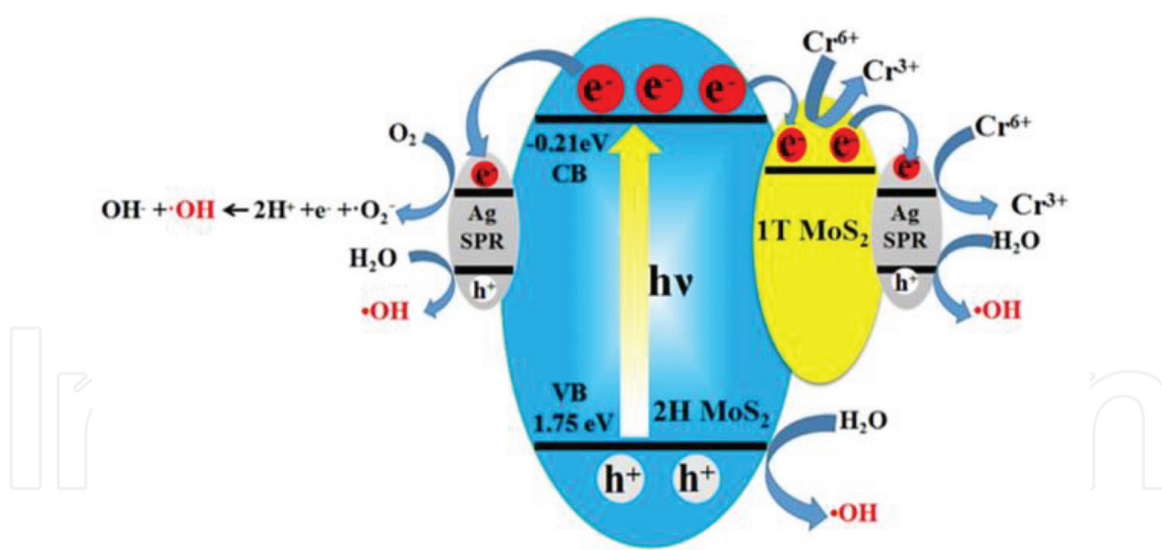


Figure 17.

Schematic illustration of photo-charge separation through 1T@2H-MoS₂/Ag under visible light irradiation. Reproduced with permission from [16].

better performance in adsorption and degradation process due to the formation of superoxide radical ($\cdot\text{O}_2^-$) and more unsaturated atoms and greater specific surface area than crystalline structure; further, the holes and hydroxyl radicals were found to be the main active substances [3].

Hongxu Guo et al. synthesized NiS nanoparticles for photocatalytic degradation and adsorption of Congo red under visible light irradiation. NiS nanoparticles were synthesized by hydrothermal method, and it exhibited efficient photocatalytic activity. 30 mg/L of Congo red was completely degraded after illumination of 210 min. In addition, OH radicals were identified by using fluorescence technique, and those highly reactive radicals were found to be the major factor for the photocatalytic process [15].

In a different study, Aniruddha Molla et al. synthesized Ag-In-Ni-S nanocomposites with different shapes for the degradation of methylene blue under dark and visible light irradiation. It is noteworthy to mention here that 20 mg of the catalyst showed a complete degradation of methylene blue within 12 min, when there was no light exposure. Notably, the degradation took only 2 min, when visible light was exposed with a 100 W lamp source. Further, the reactive oxygen species generated during the process was confirmed in their study [2].

CdS and Ni-doped CdS hollow spheres were used by Man Luo and his group for the degradation or removal of RhB and phenol. These materials were synthesized by simple template-free one-pot method. 1.2 mol% of Ni-doped CdS hollow spheres exhibited better performance in the removal of organic pollutants due to the reduce recombination rate of the electrons and hole pairs [7]. **Figure 18** illustrates the UV-absorbance profile for the degradation of RhB dye with the 1.2 mol% of Ni-doped CdS.

Earth-abundant transition metal sulfides, such as FeS₂, CuS, and NiS₂, were synthesized by fast and low-cost hydrothermal synthesis method and utilized for photocatalytic hydrogen evolution and photocatalytic degradation of indigo carmine dye under visible light irradiation. Different sacrificial agents, such as Na₂S/Na₂SO₃, EDTA, and ethanol, were used when the H₂ evolution was tested. FeS₂ showed higher activity for the hydrogen evolution ($32 \mu\text{mol g}^{-1} \text{ h}^{-1}$), and an 88% of dye (indigo carmine) degradation was attained due to their suitable electronic and optical properties. The better activity was credited to a larger crystallite size, smaller particle size, and lower recombination rate of FeS₂ than other materials

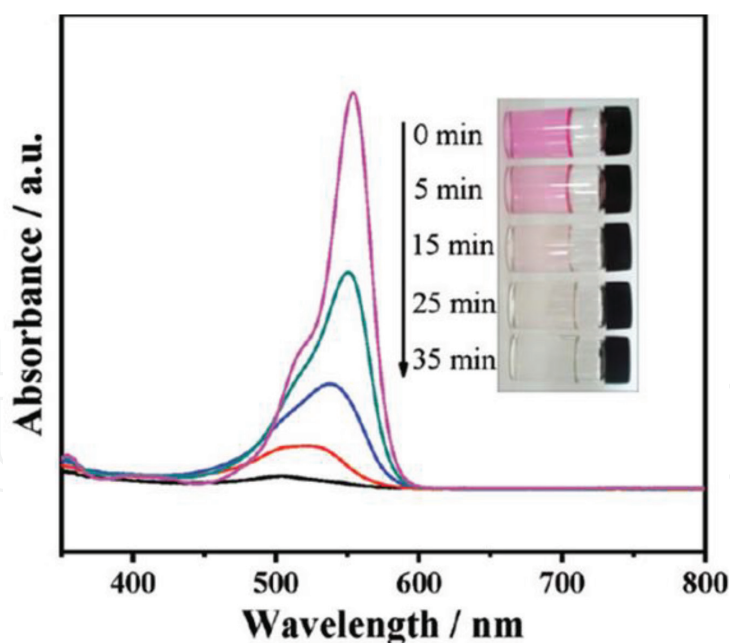


Figure 18.
 UV-visible absorption spectra of RhB in the presence of 1.2 Mol% of Ni-doped CdS. Reproduced with permission from [7].

that include CuS and NiS₂. In addition, the presence of Na₂S/Na₂SO₃ exhibited higher enhancement in the activity for the production of hydrogen among the other scavenging reagents used in this study [10].

In another study, Yongje Zhao and co-workers utilized the bimetallic chalcogenides material, FeCoS₂, synthesized by using a modulated hydrothermal method for photodegradation of methylene blue and anode materials for Na-ion batteries under UV radiation. The photocatalytic activity of FeCoS₂ which was hydrothermally treated at 190°C was found to be a better candidate with the degradation efficiency of 90% (in 150 min) under UV irradiation. The better photocatalytic activity was related with the microstructure, specific surface area, and charge separation of catalytic materials [25].

Alireza et al. prepared NiS-clinoptilolite zeolite as a catalyst via an ion-exchange and precipitation methods. The catalyst was utilized for photodegradation of furfural in aqueous solution over UV irradiation. An optimum photocatalytic efficiency was observed when 330 mg L⁻¹ of the catalyst was used at pH 5 in 6 mM of furfural solution. In addition, it was found that the degradation rate increased with increasing amount of hydrogen peroxide and potassium bromate in the solution [12].

Xi Li et al. used SnS₂ and CdS for photocatalytic degradation of different types of organic dyes, such as methyl orange (MO), Rhodamine B (RhB), Congo red (CR), orange II (OII), malachite green (MG), and methylene blue (MB), under visible light irradiation, and the activity of these two materials were compared. SnS₂ showed higher activity in the degradation of MO and lower activity in the degradation of RhB-like organic dyes, when compared to CdS material. In the degradation of azo dyes (dyes containing N=N double bond), SnS₂ followed a reduction mechanism with photoelectrons via the SnIV/SnII transition, whereas an oxidation mechanism was observed with both SnS₂ and CdS for photodegradation of organic dyes which do not consist of N=N double bond. ·O₂⁻ and ·OH radicals were found to be the major contributors for the oxidation mechanism. Since the reduction of dye molecules was faster than migration of the radicals, SnS₂ exhibited much higher activity than the CdS for the dyes containing N=N double bond. However, SnS₂ showed lower efficiency than CdS in the photocatalytic degradation of other organic dyes without N=N double bond, due to the slow production of reactive

oxidative species mentioned above. Additional experiments were carried out in the presence of the scavengers NO, N₂, O₂, and IPA [26]. **Figure 19** depicts the rate of degradation of both catalysts against the azo and non-azo dyes.

In a different study, 3D carnation flowerlike hexagonal SnS₂ nanostructures were synthesized by a simple microwave-assisted solvothermal process for photocatalytic degradation of Rhodamine (RhB) and phenol under visible light irradiation. The 3D carnation flowerlike hexagonal SnS₂ nanostructures exhibited enhanced photocatalytic

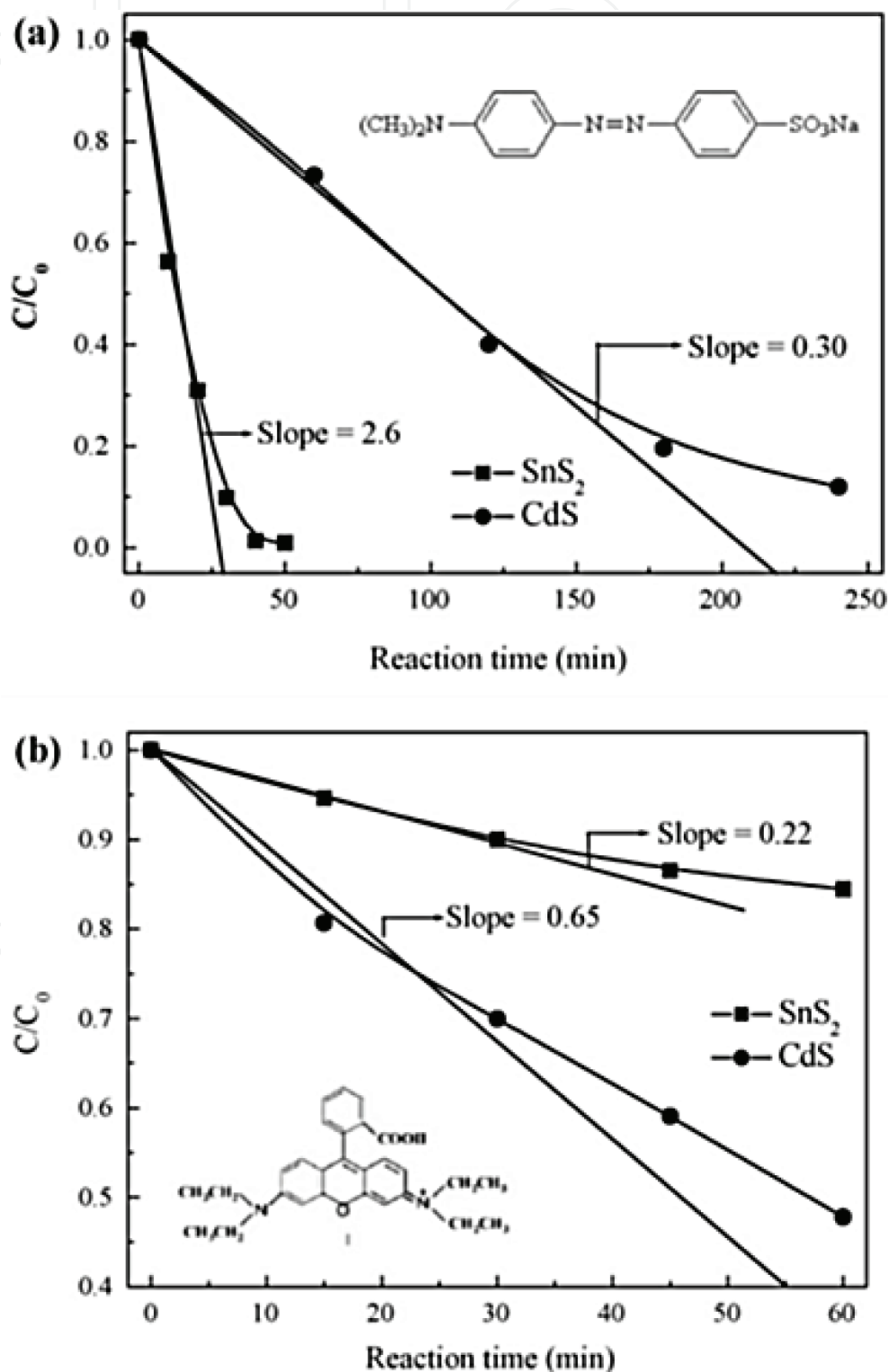


Figure 19.

Plots of normalized concentration (C_0/C) of MB vs. different time intervals (a) MO and (b) RhB photocatalytic degradation. Reaction conditions: 20 mg (a) or 50 mg (b) photocatalyst, 50 mL 6.0×10^{-5} Mol/L organic dyes, a 300 W xenon lamp (>420 nm), reaction temperature = 30°C. Reproduced with permission from [26].

activity compared to SnS_2 nanoparticles due to its high BET surface area, high surface-to-volume ratios, and increased light absorbance of hierarchical mesoporous structures [21].

Yong Cai Zhang et al. synthesized SnS_2 nanoflakes from $\text{SnCl}_2 \cdot \text{H}_2\text{O}$ for photocatalytic degradation of methyl orange (MO) under both the visible light and real sunlight irradiation. The SnS_2 material synthesized at 200°C exhibited high photocatalytic efficiency than others (i.e., 100% of degradation of MO after 60 min in the first cycle and 86% in the fifth cycle). The reason for the better degradation efficiency correlated with the combined action of several factors that include band-gap (2.21–2.25 eV), size, dispersibility, suspensibility, surface area, crystallinity, crystal defects, and photochemical stability. Almost all the materials showed better efficiency than the P25 material used for the comparison purpose [27].

SnS_2 nanocrystals with adjustable sizes were synthesized by Yong Cai Zhang and co-workers by utilizing hydrothermal method with the precursor of $\text{SnCl}_4 \cdot 5\text{H}_2\text{O}$. The materials were tested for the reduction of aqueous Cr(VI) under visible light irradiation (**Figure 20**).

It was found that the reduction of aqueous Cr(VI) depends on their hydrothermal conditions. Particularly, SnS_2 , synthesized at 150°C for 12 hours, showed highest photocatalytic activity in reducing aqueous Cr(VI) [10]. In a separate study, the same group worked on size-controlled synthesis of SnS_2 by using hydrothermal method, and their photocatalytic activity tested against the degradation of methyl orange under visible light irradiation [23].

Zhenyi Zhang et al. synthesized nanosheets of SnS_2 on $\text{g-C}_3\text{N}_4$ as 2D/2D heterojunction photocatalyst for the photocatalytic degradation of organics including dye (RhB) and phenols over visible light irradiation. It was found that the hetero-samples exhibited an enhancement in the photocatalytic degradation of organics than pure $\text{g-C}_3\text{N}_4$ and SnS_2 nanosheets. In this study, a better efficiency was attained for the catalyst loaded with 5.0 wt% SnS_2 (rate constant of $\sim 0.2 \text{ min}^{-1}$) for the RhB photodegradation [28].

Atkin and co-workers utilized two-dimensional tungsten disulfide (WS_2) nanoflakes, hybridized with carbon dots prepared using two-step method for



Figure 20.
Photodegradation of Cr(VI) in the presence of SnS_2 . Reproduced with permission from [23].

photocatalytic degradation of organic dyes. This material shows photocatalytic efficacy for the degradation of dyes. Twelve percent of degradation was obtained against the Congo red dye when 0.24 mg/L photocatalyst was utilized [29].

In another study, few layered $\text{WS}_2/\text{Bi}_2\text{MoO}_6$ heterojunction composites were prepared by Xiang Li et al. using hydrothermal method for photodegradation of organics under visible light irradiation. A higher degradation efficiency was attained by the materials further proved by the percentage removal of 99.5 and 91.7% for Rhodamine B (RhB), 98.9 and 89.8% for ciprofloxacin (CIP), 76.0 and 67.8% for methylene blue (MB), and 69.3 and 58.6% for methimazole (MMI), respectively. The reason for the removal efficiency was correlated with the structure of the materials, which may provide larger contact area for interfacial charge transfer and can shorten the migration distance of charge transfer [17] (**Figure 21**).

Hua-Bin Fang and co-workers used WS_2 nanosheets on manganese oxide (MnO_x) prepared by photo-deposition in MnSO_4 solution. Here, manganese oxide (MnO_x) was used as a hole-trapping material. MnO_x/WS_2 showed better performance in the degradation of RhB under visible light than pure WS_2 , because of the efficient charge separation in the composite promoted by MnO_x [30].

Prabhakar Vattikuti et al. synthesized 1D Bi_2S_3 nanorod/2D e- WS_2 nanosheet heterojunction by hydrothermal method for the degradation of methyl orange (MO) dye in aqueous solution and evolution of hydrogen under visible light irradiation. The material showed enhanced photocatalytic activity due to the presence of strong surface active sites and fast transfer of electron-hole pairs in the heterostructure of the composite. In addition, 84.4% of methyl orange was degraded after 90 min of exposure of visible light irradiation when 3% of $\text{Bi}_2\text{S}_3/\text{e-WS}_2$ composite was used [31].

Rajesh Bera et al. synthesized CdS nanosheet (0D, 1D, and 2D) on graphene oxide composite by surface modification method. The catalysts prepared were utilized for the photocatalytic degradation of 4-aminothiophenol under visible light. The photocatalytic activity of CdS nanosheet/RGO composite was found to nearly 4 times, 3.4 times, and 2.5 times higher than CdS nanoparticle/RGO, CdS nanorod/RGO, and pure CdS nanosheet samples, respectively. In addition, 2D-2D nanoarchitecture was found to more effective than 0D-2D and 1D-2D hybrid systems due to its better ability for harvesting of photon from sunlight and transport of excitons to their reaction sites than others [18].

Sohrabnezhad et al. worked on CoS nanoparticles supported on Al-MCM-41 material, which was synthesized by ion-exchange method. The materials were

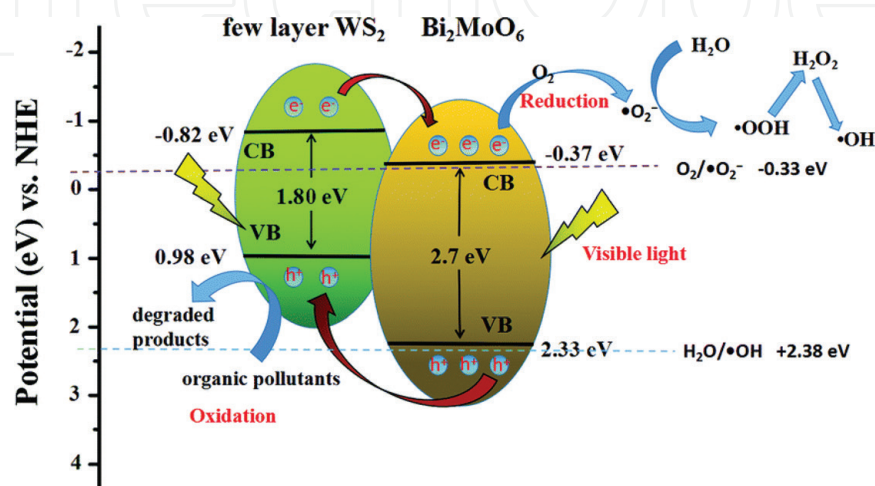


Figure 21.

Mechanism for the photocatalytic activity of $\text{WS}_2/\text{Bi}_2\text{MoO}_6$ in the presence of organic pollutants. Reproduced with permission from [17].

utilized for photocatalytic degradation of basic blue 9 or methylene blue (MB). Seven percent loading of CoS on the mesoporous support exhibited maximum efficiency for the photocatalytic degradation of methylene blue, and the optimum pH was found to be 9. The degradation followed pseudo-first-order reaction with the rate constant (k) of 0.0361. The effect of pH, amount of photocatalyst, and initial concentration of dye were also examined in their studies [11].

3. Conclusions

Metal sulfides/selenites (metal chalcogenides) have attracted considerable interest due to their electronic and optical applications. In addition, most of the common metal sulfides are nontoxic with narrow bandgap. Due to these characteristic features, metal chalcogenides have been utilized as potential candidates for photocatalysis. This chapter reviewed the most common synthetic protocol of several transition metal chalcogenides that include metal sulfides and metal selenites. Further, a brief section covered the basic characterization techniques, which have been commonly used to characterize the chalcogenide materials. Most importantly, the application of different metal chalcogenides toward environmental remediation applications, i.e., degradation of organic pollutants, is also explored herein.

Acknowledgements

The authors would like to thank the Department of Chemistry, University of Jaffna, Jaffna, Sri Lanka.

Conflict of interest


The authors declare no conflict of interests.

Author details

Sivagowri Shanmugaratnam and Shivatharsiny Rasalingam*
Department of Chemistry, University of Jaffna, Jaffna, Sri Lanka

*Address all correspondence to: srtharsha12@gmail.com

IntechOpen

© 2019 The Author(s). Licensee IntechOpen. This chapter is distributed under the terms of the Creative Commons Attribution License (<http://creativecommons.org/licenses/by/3.0>), which permits unrestricted use, distribution, and reproduction in any medium, provided the original work is properly cited. 

References

- [1] Rasalingam S, Peng R, Koodali RT. Removal of hazardous pollutants from wastewaters: Applications of TiO₂-SiO₂ mixed oxide materials. *Journal of Nanomaterials*. 2014;**2014**:10. DOI: 10.1155/2014/617405
- [2] Molla A, Sahu M, Hussain S. Under dark and visible light: Fast degradation of methylene blue in the presence of Ag-In-Ni-S nanocomposites. *Journal of Materials Chemistry A*. 2015;**3**(30): 15616-15625. DOI: 10.1039/c5ta02888d
- [3] Yang X et al. Amorphous molybdenum selenide as highly efficient photocatalyst for the photodegradation of organic dyes under visible light. *Applied Surface Science*. 2018;**457**: 214-220. DOI: 10.1016/j.apsusc.2018.06.039
- [4] Wc P, Chen Y, Li X. MoS₂/reduced graphene oxide hybrid with CdS nanoparticles as a visible light-driven photocatalyst for the reduction of 4-nitrophenol. *Journal of Hazardous Materials*. 2016;**309**:173-179. DOI: 10.1016/j.jhazmat.2016.02.021
- [5] Li Q et al. High efficiency photocatalysis for pollutant degradation with MoS₂/C₃N₄ heterostructures. *Langmuir*. 2014;**30**(29):8965-8972. DOI: 10.1021/la502033t
- [6] Liu Y et al. A highly efficient sunlight driven ZnO nanosheet photocatalyst: Synergetic effect of P-doping and MoS₂ atomic layer loading. *ChemCatChem*. 2014;**6**(9):2522-2526. DOI: 10.1002/cctc.201402191
- [7] Luo M et al. One-pot synthesis of CdS and Ni-doped CdS hollow spheres with enhanced photocatalytic activity and durability. *ACS Applied Materials & Interfaces*. 2012;**4**(3):1813-1821. DOI: 10.1021/am3000903
- [8] Zheng L, Zhang W, Xiao X. Preparation of titanium dioxide/tungsten disulfide composite photocatalysts with enhanced photocatalytic activity under visible light. *Korean Journal of Chemical Engineering*. 2016;**33**(1):107-113. DOI: 10.1007/s11814-015-0098-7
- [9] Wang Q et al. MoS₂ quantum dots @ TiO₂ nanotube arrays: An extended-spectrum-driven photocatalyst for solar hydrogen evolution. *ChemSusChem*. 2018;**11**(10):1708-1721. DOI: 10.1002/cssc.201800379
- [10] Huerta-Flores AM et al. Green synthesis of earth-abundant metal sulfides (FeS₂, CuS, and NiS₂) and their use as visible-light active photocatalysts for H₂ generation and dye removal. *Journal of Materials Science: Materials in Electronics*. 2018;**29**(13):11613-11626. DOI: 10.1007/s10854-018-9259-x
- [11] Sohrabnezhad S, Pourahmad A, Radaee E. Photocatalytic degradation of basic blue 9 by CoS nanoparticles supported on AlMCM-41 material as a catalyst. *Journal of Hazardous Materials*. 2009;**170**(1):184-190. DOI: 10.1016/j.jhazmat.2009.04.108
- [12] Nezamzadeh-Ejehieh A, Moeinirad S. Heterogeneous photocatalytic degradation of furfural using NiS-clinoptilolite zeolite. *Desalination*. 2011;**273**(2-3):248-257. DOI: 10.1016/j.desal.2010.12.031
- [13] S-H Y. Hydrothermal/solvothermal processing of advanced ceramic materials. *Journal of the Ceramic Society of Japan*. 2001;**109**(1269): S65-S75. DOI: 10.2109/jcersj.109.1269_S65
- [14] Kumar A, Pandey G. Different methods used for the synthesis of

TiO₂ based nanomaterials: A review. American Journal of Nano Research and Applications. 2018;**6**(1):1. DOI: 10.11648/j.nano.20180601.11

[15] Guo H et al. Efficient adsorption and photocatalytic degradation of Congo red onto hydrothermally synthesized NiS nanoparticles. Journal of Nanoparticle Research. 2013;**15**(3):1475. DOI: 10.1007/s11051-013-1475-y

[16] Liu H et al. Synergetic photocatalytic effect between 1 T@ 2H-MoS₂ and plasmon resonance induced by Ag quantum dots. Nanotechnology. 2018;**29**(28):285402. DOI: 10.1088/1361-6528/aabf56

[17] Li X et al. Fabrication of a novel few-layer WS₂/Bi₂MoO₆ plate-on-plate heterojunction structure with enhanced visible-light photocatalytic activity. Dalton Transactions. 2018;**47**(30):10046-10056. DOI: 10.1039/C8DT02109K

[18] Bera R, Kundu S, Patra A. 2D hybrid nanostructure of reduced graphene oxide–CdS nanosheet for enhanced photocatalysis. ACS Applied Materials & Interfaces. 2015;**7**(24):13251-13259. DOI: 10.1021/acsami.5b03800

[19] Cheng B et al. One-pot template-free hydrothermal synthesis of monoclinic hollow microspheres and their enhanced visible-light photocatalytic activity. International Journal of Photoenergy. 2012. DOI: 10.1155/2012/797968

[20] Joshi M et al. Characterization techniques for nanotechnology applications in textiles. Indian Journal of Fibre and Textile Research. 2008;**33**(3):304-317

[21] Liu H et al. Microwave-assisted solvothermal synthesis of 3D carnation-like SnS₂ nanostructures with high visible light photocatalytic activity. Journal of Molecular Catalysis A:

Chemical. 2013;**378**:285-292. DOI: 10.1016/j.molcata.2013.06.021

[22] Wang Y et al. Monolayer PtSe₂, a new semiconducting transition-metal-dichalcogenide, epitaxially grown by direct selenization of Pt. Nano Letters. 2015;**15**(6):4013-4018. DOI: 10.1021/acs.nanolett.5b00964

[23] Zhang YC et al. Size-tunable hydrothermal synthesis of SnS₂ nanocrystals with high performance in visible light-driven photocatalytic reduction of aqueous Cr(VI). Environmental Science & Technology. 2011;**45**(21):9324-9331. DOI: 10.1021/es202012b

[24] Liu P et al. Flower-like N-doped MoS₂ for photocatalytic degradation of RhB by visible light irradiation. Nanotechnology. 2016;**27**(22):225403. DOI: 10.1088/0957-4484/27/22/225403

[25] Zhao Y et al. The synthesis of FeCoS₂ and an insight into its physicochemical performance. CrystEngComm. 2018;**20**(15):2175-2182. DOI: 10.1039/C8CE00299A

[26] Li X, Zhu J, Li H. Comparative study on the mechanism in photocatalytic degradation of different-type organic dyes on SnS₂ and CdS. Applied Catalysis B: Environmental. 2012;**123**:174-181. DOI: 10.1016/j.apcatb.2012.04.009

[27] Zhang YC et al. Novel synthesis and high visible light photocatalytic activity of SnS₂ nanoflakes from SnCl₂ · 2H₂O and S powders. Applied Catalysis B: Environmental. 2010;**95**(1-2):153-159. DOI: 10.1016/j.apcatb.2009.12.022

[28] Zhang Z et al. Ultrathin hexagonal SnS₂ nanosheets coupled with g-C₃N₄ nanosheets as 2D/2D heterojunction photocatalysts toward high photocatalytic activity. Applied Catalysis B: Environmental. 2015;**163**:298-305. DOI: 10.1016/j.apcatb.2014.08.013

[29] Atkin P et al. 2D WS₂/carbon dot hybrids with enhanced photocatalytic activity. *Journal of Materials Chemistry A*. 2016;4(35):13563-13571. DOI: 10.1039/C6TA06415A

[30] Fang HB et al. Efficient charge separation promoting visible-light-driven photocatalytic activity of MnO_x decorated WS₂ hybrid nanosheets. *Electrochemistry Communications*. 2016;72:118-121. DOI: 10.1016/j.elecom.2016.09.020

[31] Vattikuti SP, Shim J, Byon C. 1D Bi₂S₃ nanorod/2D e-WS₂ nanosheet heterojunction photocatalyst for enhanced photocatalytic activity. *Journal of Solid State Chemistry*. 2018;258:526-535. DOI: 10.1016/j.jssc.2017.11.017